ROYAL SOCIETY
OF CHEMISTRY

PAPER

Check for updates

Point-of-use upcycling of 3D printing waste for developing 3D-printed Zn–I₂ batteries†

Keval K. Sonigara,[a] Jayraj V. Vaghasiya,[a] Carmen C. Mayorga-Martinez[b] and Martin Pumera [ID] *[abcd]

Three-dimensional (3D) printing technology is an effective method to fabricate and develop customized and high surface area electrodes for energy storage devices, but it also produces plastic waste and material scraps during printing and optimization. To address this issue, a more sustainable approach beyond traditional chemical recycling or landfilling is essential. In this work, we upcycle 3D printing filament scrap, specifically carbon nanofiber (CNF)/polylactic acid (PLA) composites, to develop 3D-printed rechargeable Zn–I₂ batteries (3D-ZIBs), transforming scrap into functional energy storage materials. The mechanically upcycled CNF/PLA 3D printing filaments exhibit strong chemical stability, favorable electrochemical properties, and a porous structure, enhancing iodine–iodide redox conversion as a cathode host. They also support parallel-type zinc electrodeposition, enabling long-term zinc plating/stripping with exceptional stability and corrosion resistance. The upcycled CNF/PLA-based 3D ZIB exhibits capacity (195 mA h g⁻¹) comparable to the fresh CNF/PLA electrode (197.7 mA h g⁻¹) and maintains a robust capacity retention of 78.32% after 5000 cycles. Custom designs, including micro lattice-type, brick-shaped, and ring-shaped 3D-ZIBs with gel-based catholyte/electrolyte architecture, offer functionality tailored for wearable or space-constrained applications. This study demonstrates a sustainable approach to upcycling conducting filament scrap, addressing 3D printing plastic scrap, and promoting a circular economy.

1. Introduction

3D printing is rapidly growing in various industries, including automotive, defense, manufacturing, civil engineering, and packaging, due to its ability to produce high-quality and cost-effective products.[1–3] According to market research, the 3D printing revenue was estimated at USD 17.5 billion in 2024 and is expected to grow at a compound annual growth rate of 16.4% until 2029.[4] This technology offers numerous benefits, but the generation of printing scrap negatively impacts the environment. Given its status as an emerging technology, the scrap management system has not been universally implemented due to the lack of accurate estimates regarding the types and quantities of 3D printing scrap. However, this can be understood from the

survey of fuse deposition modeling (FDM)[5] 3D-printer usage as a case study. It holds ~55.0% share in the selling market compared to other printers like stereolithography, selective laser sintering, digital light process, *etc.* (Fig. 1a).[6] The FDM method prefers to print filaments from thermoplastic polymers like PLA, acrylonitrile butadiene styrene (ABS), and other composite polymers due to their suitable fuse-deposition properties.[7,8] Among these, PLA is the most commonly used polymer, contributing significantly to the plastic scrap generation from these 3D printers (Fig. 1b).[9] According to a Filamentive report,[10] one FDM printer annually produces approximately 8.7 kg of PLA scrap. This scrap is generated during various stages of FDM printing, such as pre-nozzle filling, printing optimization, and failed or discarded prints (Fig. 1c and d). In 2022, the UK had around 132 000 printers in use, which might be an annual scrap production of ~1200 tons. However, scrap management practices vary as follows: 44% is stored, 26% is dumped, 26% is recycled, and 4% is sent to recycling services.[11] The primary obstacles are the lack of resources for recycling and the expense associated with this practice.

The chemical degradation and upcycling of PLA are economically and environmentally unfavorable (Fig. 1f). While biodegradation of PLA is a lengthy process under stringent conditions that results in the scrap being landfilled (Fig. 1g).[12,13] The most complex situations arise when the filaments are made of multiple components, such as graphene/PLA, CNF/PLA, or

[a]Future Energy and Innovation Laboratory, Central European Institute of Technology, Brno University of Technology, Purkyňova 656/123, Brno, CZ-616 00, Czech Republic. E-mail: pumera.research@gmail.com

[b]Advanced Nanorobots & Multiscale Robotics Laboratory, Faculty of Electrical Engineering and Computer Science, VSB – Technical University of Ostrava, 17. Listopadu 2172/15, 70800 Ostrava, Czech Republic

[c]Department of Medical Research, China Medical University Hospital, China Medical University, No. 91 Hsueh-Shih Road, Taichung 40402, Taiwan

[d]Department of Chemical and Biomolecular Engineering, Yonsei University, 50 Yonsei-ro, Seodaemun-gu, Seoul 03722, Republic of Korea

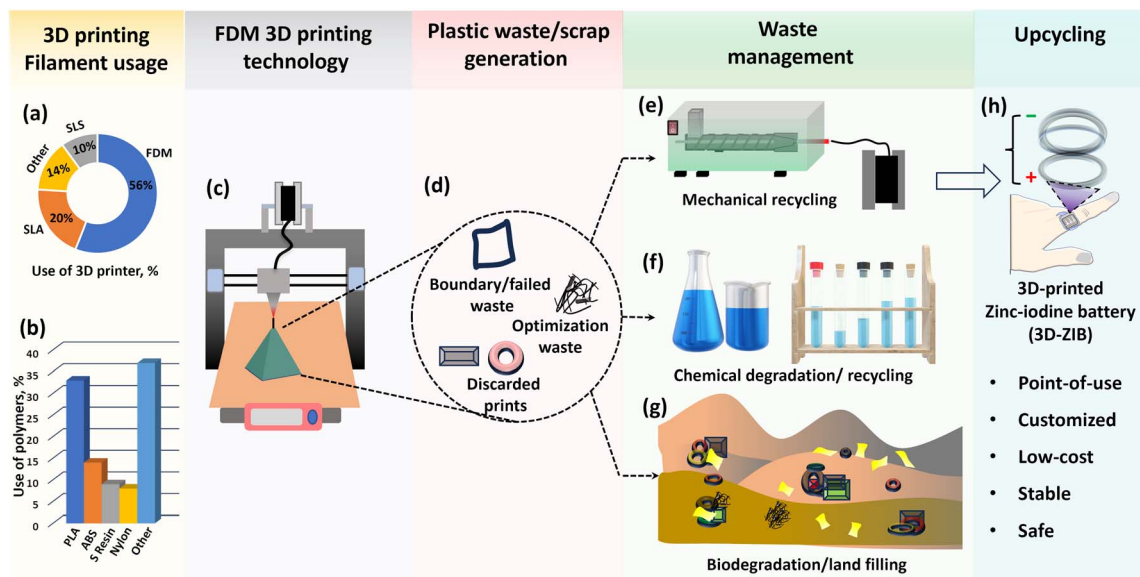† Electronic supplementary information (ESI) available. See DOI: https://doi.org/10.1039/d5ta00919g

Fig. 1 3D printing scrap generation and management. (a) % proportion of 3D printers in the market compared to FDM printers, (b) % use of polymers in FDM printing, (c) demonstration of the FDM 3D printer with PLA-based filament, (d) different types of PLA-based 3D printing scrap, (e) mechanical recycling of PLA 3D printing scrap, (f) chemical degradation/recycling of PLA, (g) disposed in land for degradation, and (h) upcycling of PLA filament scrap by the re-extruding procedure to energy storage device electrodes.

graphene/ABS, which are difficult to landfill due to the valuable composites involved. Therefore, there is a growing demand to recycle valuable materials such as metals or carbon nanomaterials in polymers using mechanical extrusion techniques (Fig. 1e).[14] Creating practical devices for energy conversion or storage through point-of-use direct upcycling could be the best approach to give such scrap a second chance and promote sustainability (Fig. 1h). Upcycling of electrode scrap offers many advantages over end-of-cycle such as no time delay, known composition, safe and effortless process, and predictable market value.[15]

FDM-printed nanocarbon/PLA materials are gaining significant interest in energy storage research due to their excellent electrochemical properties and ease of processing.[16] Since Craig *et al.* demonstrated the FDM 3D-printed graphene/PLA anode for lithium-ion batteries, it has undergone extensive study and improvement through chemical engineering efforts, leading to its integration into fully 3D-printed lithium-ion batteries.[17,18] Later, Pumera *et al.* explored it as a versatile 3D-printed substrate for wider electrochemical applications enabling the CNF/PLA surface by green activation[19] and identifying metallic impurities.[20,21] Notably, the 3D-printed carbon electrode also showed promise as a cathode host for $LiMn_2O_4$ in aqueous LIBs,[22] atomic layer-deposited V_2O_5 for zinc-ion batteries,[23] and a polymer-deposited cathode for zinc–organic batteries.[24] The activated nanocarbon/PLA and their surface modification with various polyoxometalates,[25] 2D materials like MXene,[26] VS_2,[27] and MoS_x[28] were found to be impressive for aqueous symmetric and asymmetric supercapacitors.[29] Overall, nanocarbon/PLA materials in FDM technology are expected to be tailored for large-scale industrial applications due to their versatile scope. However, these could lead to the generation of quantities of

precious material scrap on a large scale and a threat to the circular economy in the future.

Based on the above discussion and existing problems, we have selectively collected CNF/PLA filament scrap generated during the 3D printing operations in our lab and established an example of upcycling for the fabrication of 3D-ZIBs. Notably, aqueous Zn–I₂ batteries are popular for their abundant components, environmental viability, low-cost, high areal capacity, and fast charge–discharge rate.[30–33] We demonstrated the upcycling of scrap by one-step extrusion of CNF/PLA and transformed it into a 3D-printed cathode and anode host, which facilitated efficient Zn–I₂ conversion. The upcycled electrodes were found to have suitable morphology, resistivity, and electrochemical activity towards catholyte and electrolyte, which were studied by spectroscopic and electrochemical investigations. To broaden the accessibility of 3D-printed upcycled CNF/PLA, it was evaluated as a material host with liquid electrolyte in a symmetrical cell for zinc stripping/plating followed by energy storage performance with a carbon-embedded iodine cathode. A 3D-ZIB was designed with gel-catholyte (PGC) and gel-electrolyte (PGE) to demonstrate customized and wearable shapes. This configuration exhibits excellent control over self-discharge and demonstrates long-term cycling stability. The *in situ* spectroscopy reveals facile iodine–iodide conversion and reversible electrochemistry. As a practical demonstration, ring- and brick-shaped ZIBs were fabricated, which reflect the future possibilities of wearable and point-of-use energy storage devices.

2. Results and discussion

2.1 Upcycling of CNF/PLA scrap to ZIB electrodes

The carbon scaffolds are the most suitable conductive support for facile iodine redox chemistry and smooth stripping/plating

This journal is © The Royal Society of Chemistry 2025

J. Mater. Chem. A, 2025, **13**, 11804–11816 | **11805**

of zinc in ZIBs.[34–37] Considering this fact, we selectively collected the CNF/PLA filament scrap generated during FDM printing in the lab to conduct an upcycling study. A digital image of the collected CNF/PLA 3D printing scrap is provided in Fig. S1a.† Subsequently, it underwent grinding and extruding procedures without any pre-treatment to produce upcycled CNF/PLA filaments with precise dimensions (see Fig. S1a–d,† and detailed

procedure in the Experimental section). We found that 96.3% of scraps was successfully transformed into filaments by the extrusion procedure. The printability of upcycled CNF/PLA was verified by differential calorimetry analysis, and a melting event was identified at ~162 °C, which aligned with the PLA fused deposition printing range (Fig. S2†). Composition plays a pivotal role, particularly in nanocarbon/PLA composites, when
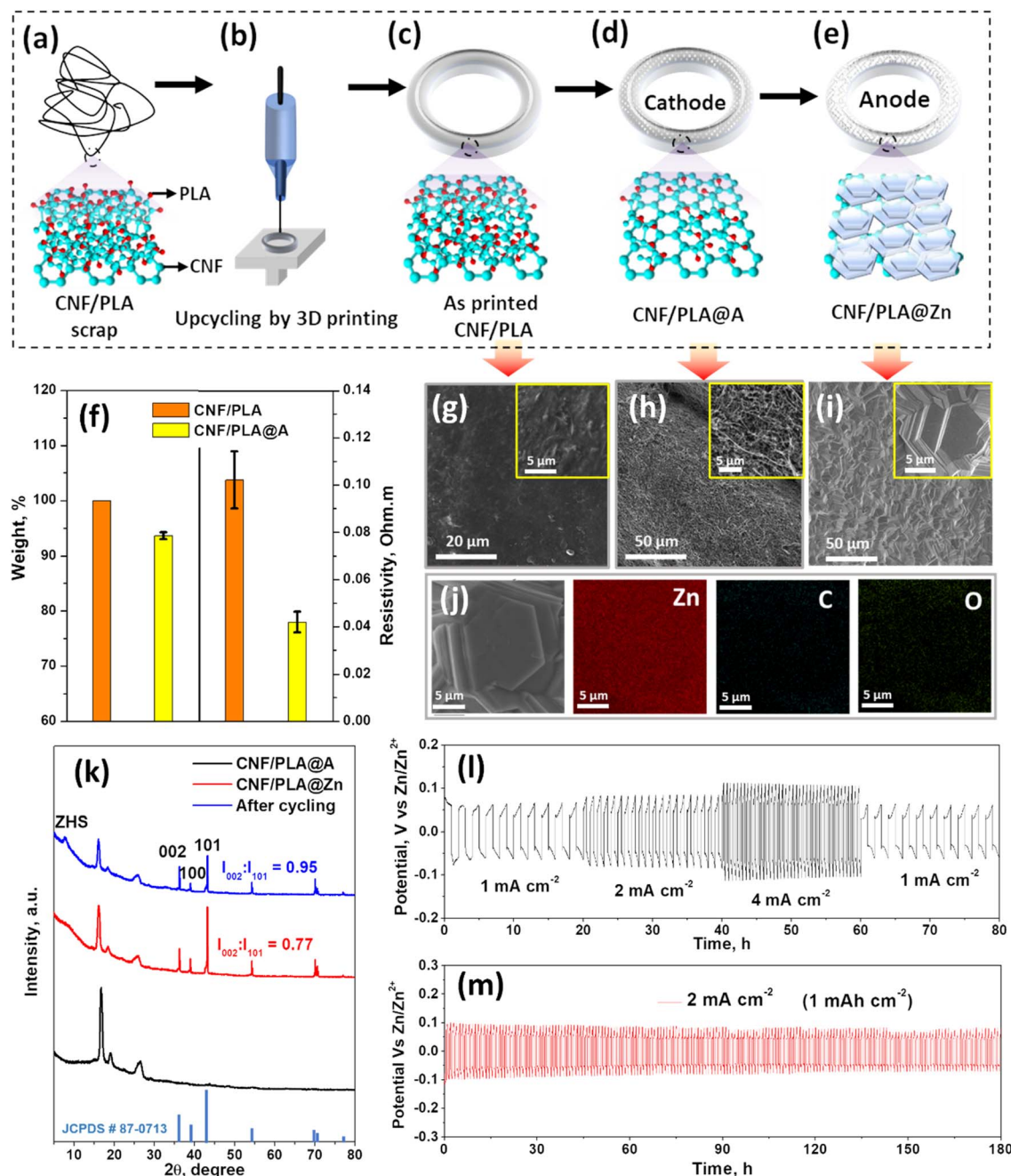

Fig. 2 3D printing CNF/PLA scrap upcycling to 3D electrodes for ZIBs: (a) collected CNF/PLA filament scrap from the 3D printing unit, (b) upcycling and 3D printing of filament scrap to point-of-use shape electrodes, (c) as-printed CNF/PLA in a ring shape, (d) chemical activation by surface removal of PLA to be used as a cathode (CNF/PLA@A), (e) electrodeposition of zinc metal on the activated electrode for anode preparation (CNF/PLA@Zn), (f) PLA weight loss and decrease in resistivity by chemical activation, (g–i) SEM images of as-printed CNF/PLA, CNF/PLA@A and CNF/PLA@Zn, (j) EDS mapping of CNF/PLA@Zn, (k) XRD patterns of CNF/PLA@A, CNF/PLA@Zn, and CNF/PLA@Zn after 360 h of stripping/plating, (l) zinc stripping/plating profiles of CNF/PLA/Zn at 1 mA h cm^{-2} and different rates, and (m) long-term stripping/plating profile at 2 mA cm^{-2} for 180 h. Note: error bars represent average deviation.

11806 | J. Mater. Chem. A, 2025, 13, 11804–11816

This journal is © The Royal Society of Chemistry 2025

it comes to upcycling. A comparison of thermogravimetric mass loss between pure PLA and upcycled CNF/PLA indicated a CNF content of approximately 13.5 wt% in the upcycled filament (Fig. S3†). X-ray photon spectroscopy (XPS) was carried out to study the chemical stability and surface composition retention of fresh and upcycled CNF/PLA (Fig. S4†). The spectra reflect a deviation of less than 3% in the atomic proportions of carbon and oxygen after upcycling. Subsequently, this upcycled filament was utilized for printing electrodes in various point-of-use shapes and sizes, including circular discs, rings, and brick shapes.

The schematic of the upcycling procedure from the scrap to cathode and anode fabrication is provided in Fig. 2a–e. The upcycled CNF/PLA undergoes three steps, 3D printing (as-printed CNF/PLA (Fig. 2c)), chemical activation (CNF/PLA@A as the cathode (Fig. 2d)) and zinc electrodeposition (CNF/PLA@Zn as the anode (Fig. 2e)). For electrochemical devices, electrical conductivity of electrodes is a key parameter that directly influences their performance, thus necessitating evaluation. As shown in Fig. 2f (right side), the as-printed CNF/PLA has significantly low resistivity due to the 3D network of highly conducting CNF fillers. To enhance the compatibility of CNF/PLA with aqueous electrolytes and electrochemistry, it is necessary to remove the surface PLA to expose the conducting CNF surface by a process called chemical activation that results in CNF/PLA@A. The as-printed CNF/PLA was treated with NaOH solution to degrade PLA from the surface, resulting in a successive decrease in resistivity (Fig. 2f right side) with a minimal loss of PLA (~6 wt%) and retaining ~94% of PLA for utilization in CNF/PLA@A (Fig. 2f, left side). For the demonstration of sufficient conductivity of activated CNF/PLA@A, it was used as an electrical contact to complete the light-emitting diode powering circuit (Fig. S5†). It indicates good electronic conduction through a 3D-printed CNF/PLA@A frit and can be used in electronic devices or as an electrode.

To gain better insight into morphology, electrodes were studied by scanning electron microscopy (SEM), energy-dispersive spectroscopy (EDS), and X-ray diffraction (XRD). The SEM image of the as-printed CNF/PLA electrode revealed CNF covered with PLA (Fig. 2g). In contrast, the CNF/PLA@A electrode showed a porous CNF network after successfully removing the surface PLA (Fig. 2h). The fiber structure on the surface of the electrode enhanced the contact area, providing an ideal platform for ion diffusion. XPS was used to know about surface composition changes during the activation of CNF/PLA (Fig. S6a†). The XPS spectra revealed the presence of titanium (0.54 wt%) and sodium (0.49 wt%) in CNF/PLA@A along with carbon and oxygen. Sodium impurities could be formed due to salt formation in the PLA chains during NaOH treatment.[38] The presence of titania is related to inherent impurities in CNF, which was also observed in a previously reported study.[20] The deconvolution of the Ti 2p orbital suggests that titanium is in the oxide state (Fig. S6b†). Metal oxides like TiO_2 are well known for their stability in iodide–triiodide redox electrolytes used in photoelectrochemical cells,[39] which may not be a threat to use in ZIBs.

Fig. 2i shows the SEM image of CNF/PLA@Zn. The observed microplates exhibit a smooth and uniform morphology with parallel crystal growth, indicating favorable properties for ZIBs. EDS confirms the presence of Zn along with C and O elements throughout the electrode (Fig. 2j). Notably, the proportion of zinc was found to be 95.0 wt%, without the formation of sulfates, as revealed by the EDS spectrum, confirming the high purity of deposition (Fig. S7†). The XRD results of zinc deposition show three characteristic peaks corresponding to crystal planes 002, 101, and 100 for pure metallic zinc matching with JCPDS 87-0713, as mentioned in Fig. 2k. The ratio between 002 : 101 crystalline planes is 0.77 and suggests a good proportion of parallel type zinc crystal orientation. This result supports the SEM observations of CNF/PLA@Zn morphology. This parallel crystal growth suggests tight zinc deposition, making it ideal for minimizing dendrite formation in ZIBs.[40] Before using CNF/PLA@Zn in ZIBs, it was electrochemically tested in a symmetrical cell with 2 M $ZnSO_4$ electrolyte to analyze the stripping/plating performance of zinc and its stability as an anode. The controlled voltage polarization during stripping/plating at 1.0 mA h cm^{-2}, across varying current densities ranging from 1 mA cm^{-2} to 4 mA cm^{-2}, demonstrates stable characteristics, which are crucial for ZIBs (Fig. 2l). Additionally, the electrode underwent long-term cycling for 180 h at 2 mA cm^{-2} and 1 mA h cm^{-2}, and it stabilized very well over the cycling study with reduced polarization (Fig. 2m). Furthermore, the stability test was extended at a high rate of 4 mA cm^{-2} for a long run of 360 h to validate stable stripping/plating (Fig. S8†). These tests confirm the stable stripping/plating behavior at different rates and over a long time duration that benefits the overall stability of ZIBs. The XRD analysis of cycled CNF/PLA@Zn reveals intact characteristic peaks corresponding to zinc planes with an improved 002 : 101 ratio of 0.95 (Fig. 2k). This indicates good corrosion tolerance of parallel-type zinc deposits. However, the trace amount of corrosion observed from the new peak arises at a 2θ value of ~8°, attributed to zinc hydroxide sulfate (ZHS) formation. This by-product formation is the result of a mild acidic electrolyte medium which triggers a hydrogen evolution reaction and tends to increase hydroxide ion concentration at the anode surface. Following pH change, the zinc anode reacts with water, sulfates, and hydroxides to give the corrosion product ZHS ($4Zn^{2+} + 6OH^- + SO_4^{2-} + xH_2O \rightarrow Zn_4SO_4(OH)_6 \cdot xH_2O$).[41] The SEM image of cycled CNF/PLA@Zn suggests the good retention of compact and uniform morphology with controlled traces of corrosion (Fig. S9†). Overall, the anode performance is recommended for use in ZIBs based on good stripping/plating and controlled corrosion of CNF/PLA@Zn.

2.2 Performance of upcycled 3D electrodes in conventional ZIBs

To evaluate the performance of 3D-printed electrodes in conventional ZIBs, disc-shaped CNF/PLA@A and CNF/PLA@Zn were designed. The fresh and upcycled CNF/PLA@A was coated with iodine-loaded carbon and cycled in a liquid electrolyte environment. The galvanostatic charge–discharge (GCD) profiles between 0.6 V and 1.6 V at 0.25 mA g^{-1} are presented in

This journal is © The Royal Society of Chemistry 2025

J. Mater. Chem. A, 2025, **13**, 11804–11816 | **11807**

Fig. 3a, which shows a typical GCD profile of ZIBs with specific discharge capacities of 195.0 mA h g^{-1} and 197.7 mA h g^{-1} for upcycled and fresh electrodes, respectively. Fig. 3b and c summarize the rate performance of upcycled and fresh electrodes, respectively, from 0.25 mA g^{-1} to 10 mA g^{-1}, which follows a similar trend with different current densities and good capacity recovery. The coulombic efficiency (CE) is intact at different current rates and achieves values above 99%, which ensures effective Zn–I$_2$ conversion during GCD cycles. Both electrodes show comparable performance and conclude the effectiveness of the upcycled strategy to retain good electrochemical properties. To validate redox conversion and kinetics in ZIBs, cyclic voltammetry (CV) curves were measured at different scan rates for the upcycled electrode (Fig. 3d). The oxidation and reduction peaks correspond to the iodine–iodide redox conversion, as seen in ZIB studies.[34–37] The redox peaks are very stable over an increase in the scan rate that shows good redox stability.

The redox kinetics can be understood from the relationship between the CV peak current and scan rate based on the power law ($i_p = av^b$), where the peak current i_p is related to the scan rate v, while a and b represent variables. In the linear logarithmic plot of i_p and v, the slope value b of 0.5 indicates a diffusion-controlled process, and the slope value b of 1.0 indicates a capacitive process. This linear relationship for anodic and cathodic peaks is provided in Fig. S10a and b†, which yields b values of 0.58 during oxidation and 0.72 during reduction. These values indicate the combination of capacitive-controlled and capacitive energy storage in the present system iodide–iodine redox reaction. The ratio of both processes at different scan rates is summarized in Fig. 3e, derived based on the following equation, $i(V) = k_1v + k_2v^{1/2}$, where k_1 is the capacitive contribution and k_2 is the diffusion-controlled contribution.[47] The capacitive contribution is 59.71% at 0.25 mV s^{-1}, which increases to 70.09% at 1.25 mV s^{-1}, suggesting a favorable conductive electrode for faster iodine/iodide conversion. Such redox conversion can be identified through the oxidation state of iodine at the cathode surface by an XPS study, as shown in Fig. S11.† The as-fabricated electrode results in two pairs of I 3d orbitals at binding energies (B.E.) of ∼ 619 eV (3d$_{5/2}$) and ∼631 eV (3d$_{3/2}$), attributed to the loaded elemental iodine in carbon, while splitting at a lower B.E. is attributed to iodide formation through charge transfer to the carbon host. In the case of the discharge electrode, the iodine peak is lowered
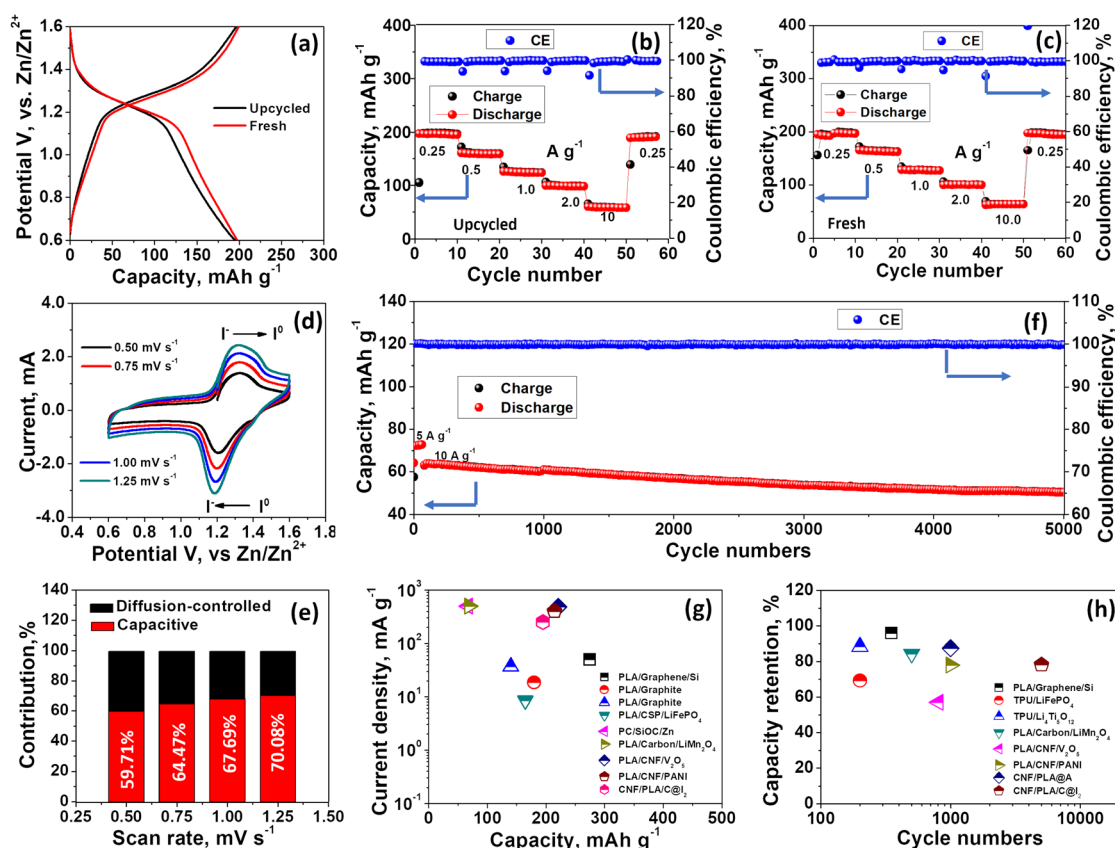

Fig. 3 Performance of conventional 3D ZIBs. (a) GCD profiles, (b and c) rate performance of the upcycled electrode and fresh electrode, respectively, (d and e) CV curves at different scan rates and the corresponding ratio of capacitive- and diffusion-controlled contributions, respectively, (f) long-term stability profile of the upcycled electrode at 10 A g^{-1}, and (g and h) comparison of capacity and stability performances of the upcycled electrode with other reported FDM printed zinc-ion and lithium-ion batteries, respectively. Electrodes and reference for comparison: PLA/carbon/LiMn$_2$O$_4$,[22] PLA/CNF/V$_2$O$_5$,[23] PLA/CNF/PANI,[24] PLA/graphene/Si,[42] PLA/graphite,[43] PLA/CSP/LiFePO$_4$,[44] PC/SiOC/Zn,[45] TPU/Li$_4$Ti$_5$O$_{12}$,[46] TPU/LiMn$_2$O$_4$,[46] CNF/PLA/C@I$_2$ and CNF/PLA@A [this work].

11808 | *J. Mater. Chem. A*, 2025, **13**, 11804–11816

This journal is © The Royal Society of Chemistry 2025

and is shifted to iodide, while in the charged electrode, the iodine peak emerges again and a decrement in the iodide peak is observed. The XPS study suggests a facile iodine/iodide conversion reaction.

Long-term stability is a crucial factor for studying the battery performance. Fig. 3f illustrates the long-term cycling of the upcycled electrode at 10 mA g^{-1}, exhibiting 78.32% capacity retention after 5000 cycles. The capacity decay is related to zinc corrosion over cycling, attributed to byproduct or dendrite formation, as observed in the symmetrical cell study. It is an inherent phenomenon in ZIBs.[41] For stability confirmation of the cathode, surface morphology was studied for the as-fabricated cathode and after long-term charge–discharge cycling (Fig. S12a and b†). The study reveals high surface stability of CNF/PLA@A while charge–discharge cycling with comparatively rough and passivated surface due to deposition and dissolution activities. Overall, the capacity performance and stability of the presented upcycled 3D-printed CNF/PLA@A based ZIB is comparable/superior to the reported battery capacity and stability performance of nanocarbon/PLA-based 3D-printed cathode/anodes in lithium-ion and zinc-ion batteries (Fig. 3g and h).[22–24,42–46] The study unveils that the upcycled CNF/PLA with 3D structures are suitable and excellent electrodes for aqueous batteries that are more sustainable and safer. They can be utilized further due to their lattice-type high-surface area, arbitrary, or customized shapes for use in wearable and grid-scale design-oriented energy storage systems. However, this needs a specific gel/solid-state electrolyte and electrode engineering to realize the robust use of leakage-free and point-of-use application-oriented devices.

2.3 Performance of upcycled 3D electrodes with polymer gel catholyte

Aiming to achieve customized shape and leakage-free ZIBs for practical use, upcycled 3D electrodes are utilized in modified battery engineering using an aqueous polymer gel catholyte (PGC) with pre-embedded iodide–triiodide (KI/I$_2$) and an aqueous polymer gel electrolyte (PGE). PGC and PGE were developed in 35 wt% polyethylene-oxide–polypropylene oxide copolymer scaffolds (PEO–PPO–PEO) based on previously used ZIBs (for details, please see the Experimental section).[48–50] The CNF/PLA@A directly functions as an iodine-free cathode and CNF/PLA@Zn as an anode. Fig. 4a and b illustrate the ZIB assembly, components, and its working mechanism during charge–discharge cycles. Fig. 4c shows the CV curves of the ZIB in the potential range of 0.6 V to 1.8 V at different scan rates from 0.50 mV s^{-1} to 1.25 mV s^{-1}. During the oxidation scan, two distinct peaks are observed at 1.30 V (I$^-$ to I$_3^-$) and 1.47 V (I$_3^-$ to I$_2$). These peaks correspond to the formation of tri-iodide species, which subsequently transform to iodine by the oxidation process and transform into polyiodide in the presence of iodine generated at the cathode surface. On the other hand, during the reduction scan, the CV curve exhibits a pronounced reduction peak at 1.09 V (I$_2$ to I$_3^-$) and a second, shallower peak at 0.93 V (I$_3^-$ to I$^-$). These reduction features are associated with the reversible formation of iodine to iodide in the system. The

redox procedure of two-step iodine/iodide matches well with the documented Zn–I$_2$ battery chemistries.[49,51] The efficient Zn–I$_2$ redox reaction occurring at CNF/PLA@A indicates a sufficient electronically conductive environment and a higher open surface area for interaction. The linear and reversible increase in oxidation and reduction peaks at lower to higher scan speeds suggests faster iodide/iodine conversion.[47]

The GCD curves replicate the similar redox plateau observed in the CV study (Fig. 4d). The ZIB cycled at 0.5 A g^{-1} gives a capacity of 172.16 mA h g^{-1} that realizes an energy density of 201.4 W h kg^{-1}. The major capacity contribution in the discharge curve delivered from the flat voltage plateau of ∼ 1.2 V indicates fast kinetics at solid–gel interfaces and sufficient ionic mobilities in gel media. The rate performance summarizes the capacity and coulombic efficiency from 0.5 A g^{-1} to 10 A g^{-1} (Fig. 4e). While increasing the rate up to 10 mA g^{-1}, it retains a capacity of 60.6 mA h g^{-1} with nearly 99% coulombic efficiency and restores the initial capacity at 0.5 A g^{-1}. Overall, the solid–gel interface-based 3D-ZIB approach is practical like a conventional liquid electrolyte battery. Notably, the energy storage performance is higher or comparable to reported gel electrolyte-based aqueous Zn–I$_2$ batteries.[49,52–55]

The mechanism of Zn–I$_2$ conversion was studied to understand redox reactions at the CNF/PLA@A and PGC interface. As described in Fig. 4a and b, iodide/triiodide present in PGC form iodine and polyiodides during charging at the CNF/PLA@A surface. This process is similar to that reported in recently developed ZIBs.[33,34,49] Fig. 4f shows in situ Raman spectra of the CNF/PLA@A and PGC interface, which detect a major dominant peak at 110.23 cm^{-1}, attributed to the triiodides present in the PEO–PPO–PEO gel matrix at open circuit potential (∼1.2 V vs. Zn/Zn^{2+}).[49] During the initial charging cycle (from 1.2 V to 1.6 V), a new peak is observed at 165.23 cm^{-1}, attributed to linear I$_5^-$. These I$_5^-$ are generated due to the formation of iodine at the CNF/PLA@A surface, where it reacts with I$_3^-$ and forms I$_5^-$ (I$_2$@I$_3^-$).[34,56] The observed phenomenon is quite similar to the reported Raman study of iodine in I$^-$ or I$_3^-$ media that form the corresponding poly-iodides.[57,58] The I$_5^-$ peak continuously increases up to 1.6 V, indicating instantaneous iodine formation during charging. In the discharging step (Fig. 4g), a reversible trend of this peak is observed, where the I$_5^-$ peak starts decreasing and vanishes at discharge. This confirms iodide formation from iodine. Furthermore, the second charge cycle validates the re-formation of I$_5^-$ at 1.6 V charge of the ZIB (Fig. 4h). Raman spectroscopy reveals facile and reversible redox conversion in the present ZIB. The cathode surface was also investigated by XPS analysis of the I 3d orbital of the as-fabricated, charged, and discharged CNF/PLA@A (Fig. S13†). The as-fabricated electrode does not show any peak of iodine; after charging, it displays iodine/iodide peaks with pronounced iodides, due to the plating of iodine from the PGC electrolyte, which forms polyiodides as observed in the Raman study. In the discharged electrode, the iodide peak is increased, while the iodine peak nearly vanishes, which confirms the conversion of iodine to iodide. The investigation concludes that introducing an upcycled 3D-printed CNF/PLA@A cathode provides a suitable conductive surface to host the Zn–I$_2$ redox reactions.

This journal is © The Royal Society of Chemistry 2025

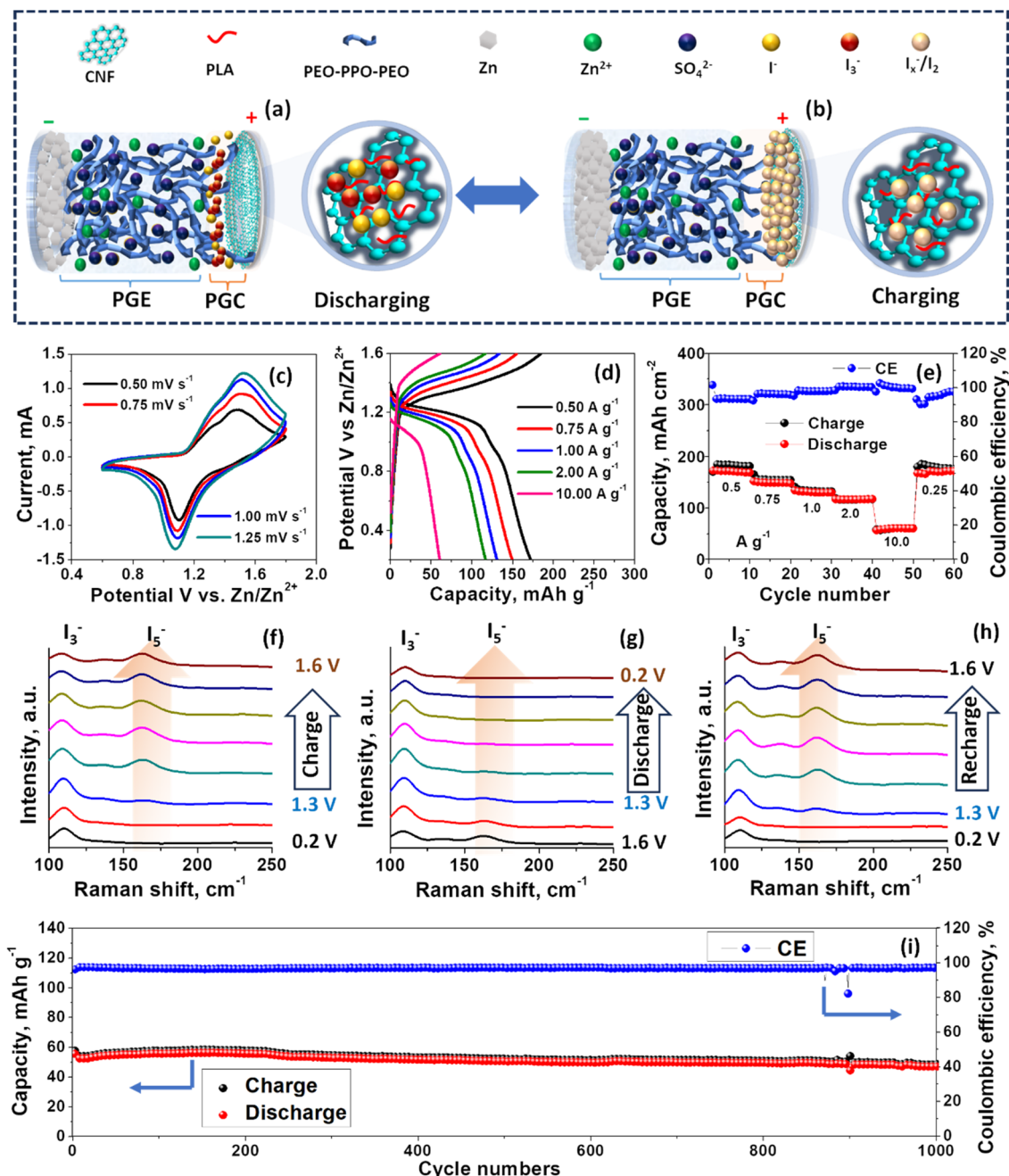J. Mater. Chem. A, 2025, **13**, 11804–11816 | **11809**

Fig. 4 Electrochemical study of 3D electrodes in PGC/PGE and the conversion mechanism: (a) 3D-ZIB in the discharge condition with a sandwiched PGC/PGE interface, (b) 3D-ZIB in the charge condition. (c) CV performance at different scan rates, (d and e) GCD and rate performances, (f–h) *in situ* Raman spectra of the electrode–electrolyte interface during charge–discharge and recharge, and (i) long-term stability at 10 A g^{-1}.

The long-term cycling stability of the ZIB was studied for 1000 cycles, which retained a stable energy efficiency and realized 87.58% capacity retention (Fig. 4i). The impressive stability of this ZIB is associated with the controlled diffusion phenomenon of the iodides during charge–discharge. To confirm this, we studied the self-discharge of the ZIB for different intervals of 10 h, 20 h, and 30 h to evaluate capacity loss during the rest period (Fig. S14†). After every rest period, the ZIB achieved above ∼99% coulombic efficiency without loss of capacity. The ZIB realized a minimum self-discharge rate of 4.3 mV h^{-1}, which is comparable with the best-reported self-discharge-controlled ZIBs.[59] This significant self-discharge control may be reasonable from a gel-type catholyte having oxygen-functionalities in the PEO–PPO–PEO copolymer scaffold.[60] Even at controlled iodide diffusion, noticeable capacity loss is still observed. To understand this, the *ex situ* SEM and EDS elemental mapping analysis were done (Fig. S15 and S16†). The corresponding EDS spectrum with elemental mapping revealed the presence of sulfur in the cycled CNF/PLA@Zn surface composition, validating the capacity decay associated

11810 | *J. Mater. Chem. A*, 2025, **13**, 11804–11816

This journal is © The Royal Society of Chemistry 2025

with ZHS byproduct formation, as observed in the initial cycling study of zinc symmetrical cells. This corrosive product forms an insulating layer at the surface and reduces the ion transport to the zinc surface, which leads to sluggish energy storage conversion. Such corrosion can be overcome by reducing water activity in electrolytes and interfaces through additive engineering or anode modification with a protective coating.[30,31,45] Surface morphology was analyzed with SEM for the as-fabricated and cycled electrode to study the effect of charge–discharge on the stability of the cathode (Fig. S17a and b†). Compared to the as-fabricated electrode, morphologies of the cycled electrode were observed with less pores and bearing traces of PGC and depositions. However, electrode morphology is identical to the as-fabricated electrode in terms of uniformity, which suggests good stability over charge–discharge. Overall, the quality and performance of upcycled CNF/PLA indicates its suitability for a range of conversion-type cathodes for future batteries.

2.4 Proof-of-concept for lattice-structured and ring- and brick-shaped 3D-ZIBs

The key advantage of 3D-printed electrodes is their ability to form customized shapes using scalable methods, making the developed 3D ZIBs from upcycled CNF/PLA adaptable to specific power supply needs. Fig. 5a inset shows a digital image of a micro-structured lattice-type CNF/PLA@A electrode with an expanded SEM image, confirming the good resolution of FDM printing. The electrode after PGC infusion shows high loading through micro-structured voids in lattice patterns that avail high-surface area (Fig. 5, inset). Fig. 5a and b show the GCD curve and stability performance, respectively. It delivered a capacity of 120.1 mA h g^{-1} at 1 A g^{-1} and 65.21% after 2000 cycles with stable CE performance, suggesting the potential of lattice-type printing for high-loading applications. As a proof of concept, we designed ring- and brick-shaped ZIBs with similar volumes and evaluated their performance. Fig. 5c describes CNF/PLA@A electrodes in a ring shape with concave- and
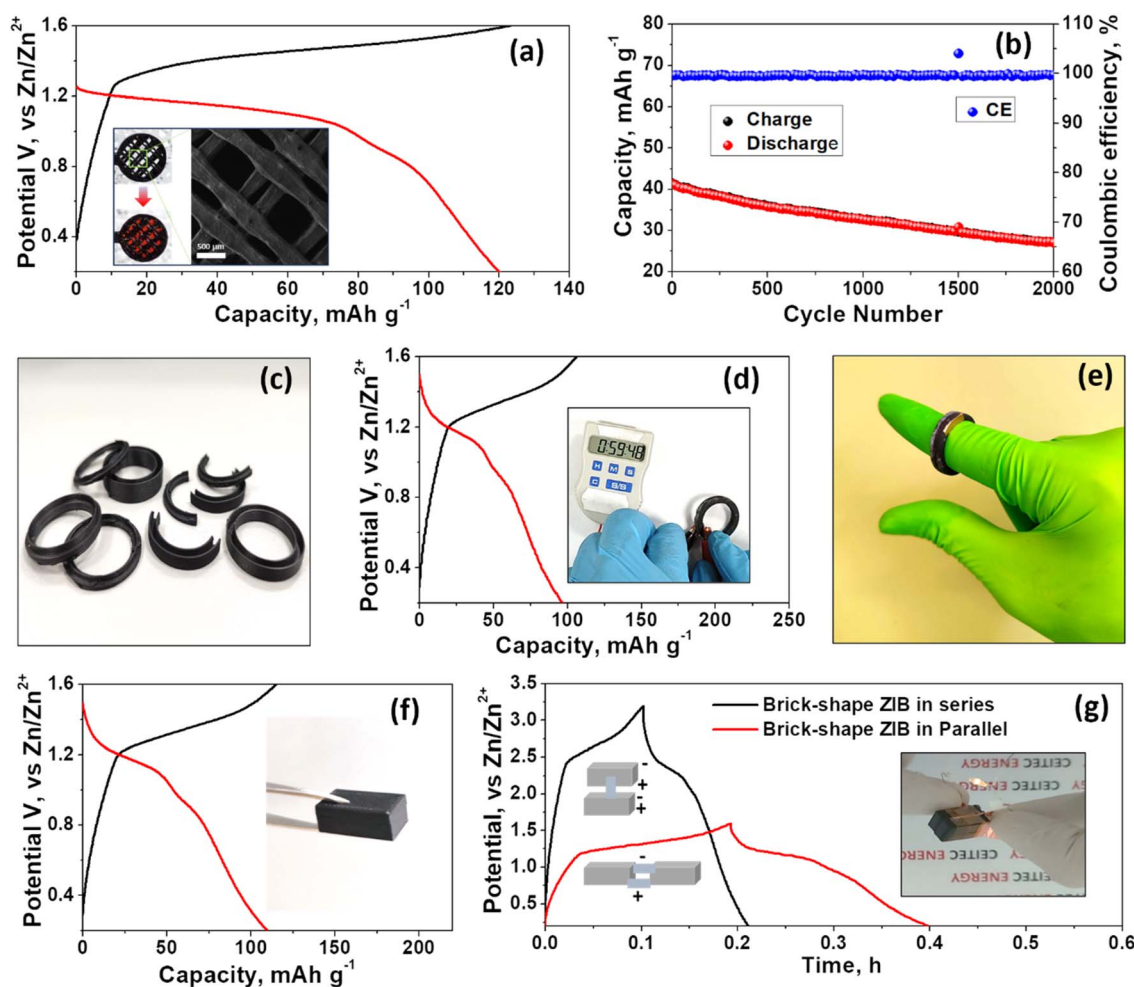

Fig. 5 3D-ZIB prototype designs and its applications: (a) GCD performance of the lattice-type electrode; inset is a digital image of the electrode and SEM image, (b) long-term stability at 10 A g^{-1}, (c) digital images of ring-shaped electrodes, (d) GCD performance at 1 A g^{-1}; the inset shows powering a digital clock with a ring-shaped ZIB, (e) wearable demonstration of the ring-shaped ZIB. (f) GCD profile of the brick-shaped ZIB at 1 A g^{-1}; the inset shows its digital photograph, (g) GCD profile of the brick-shaped ZIBs in series and parallel configuration; the inset shows powering a white light-emitting diode using a series configuration of two brick-shaped ZIBs.

This journal is © The Royal Society of Chemistry 2025

J. Mater. Chem. A, 2025, 13, 11804–11816 | 11811

convex-type geometries and indicates the possibility of minia-tured designs. Fig. S18† shows the fabrication of the ring-shaped CNF/PLA@Zn, confirming that smooth, arbitrary-shaped anode electrodeposition is feasible. The ring-shaped ZIB results in an open circuit voltage of 1.21 V vs. Zn/Zn^{2+} and delivers 96.66 mA h g^{-1} specific capacity (116.95 mA h cm^{-3}) with an identical discharge curve, which is slightly polarized to the mid-discharge potential of 0.97 V vs. Zn/Zn^{2+} (Fig. 5d). It can produce sufficient current and voltage (above 1 V) to power the digital clock for more than 16 h on a single charge (inset; Fig. 5d). The demo of powering a digital clock can be found in Movie S1.† Fig. 5e shows the wearability of ring-shaped ZIB.

Furthermore, miniature brick-shaped electrodes were prin-ted with the bottom part as the cathode and the top one as the anode (Fig. S19a†). The brick-shaped battery delivered 109.78 mA h g^{-1} specific capacity (137.15 mA h cm^{-3}) with a coulombic efficiency of 96% (Fig. 5f). For powering a light-emitting diode (voltage requirement is more than 1.6 V), the discharge profile of single brick-shaped ZIB was inefficient. Hence, GCD profiles of brick modules of two ZIBs in series and parallel connections were studied to get an insight into their energy storage performance (Fig. 5g). The two batteries in parallel series were cycled, where the charge–discharge time of the module was double that of the single one while maintaining a similar operating potential. In a series connection, the oper-ating voltage of the module was nearly doubled (3.2 V) compared to a single ZIB with a mid-discharge voltage of ~2.0 V. It was able to power the white light-emitting diode for several minutes (inset of Fig. 5g and Movie S2†).Thanks to the straightforward material properties and the capabilities of FDM printers, it is feasible to achieve batch-scale production of multiple devices. The ability to print multiple electrodes in a single batch has been successfully demonstrated (Fig. S19b†). The present upcycling strategy removes the traditional material recycling procedures and tedious treatments, additives, and binders that are utilized during the manufacturing of upcycled devices. This report introduces a good start to upcycling 3D conducting filaments or active materials filaments with a ther-moplastic polymer composite for developing sustainable energy storage devices. It is also possible to extend such upcycling towards the development of other popular FDM-compatible composite polymers such as polyurethanes[61] and tere-phthalate[62] and their carbon composite for upcycled metal-ion battery electrodes.

3. Conclusion

In summary, we demonstrated an engineering way to utilize 3D printing CNF/PLA scrap with direct upcycling to develop the 3D-ZIB using FDM printing technology. The thermal, morpholog-ical, and electronic property investigation of upcycled CNF/PLA suggests good chemical inertness and retaining preferred printability. During mechanical upcycling, more than 93% of PLA was recycled in the backbone of 3D-printed electrodes. The 3D-ZIB based on an upcycled cathode (CNF/PLA@A) and anode (CNF/PLA@Zn) provides substantial capacity, capacity reten-tion, and outstanding rate performance. The detailed Raman

spectroscopic evaluations confirm the reversible iodide–iodine formation reactions via I_3^-/I_5^- intermediates at the surface of the 3D-printed CNF/PLA cathode. Notably, the 3D-ZIB achieved ultra-low self-discharge due to the efficient role of PGC and PGE, which control the diffusion. Finally, the emergence of 3D-ZIBs in lattice, ring, and brick shapes justifies fabrication approaches for crafting arbitrary-shaped 3D-ZIBs for various applications. The integrated ZIBs in the module perform with the expected above ~2 V discharge potential over the added device in a series connection to power electronic gadgets. This 3D-ZIB can be a safe alternative to existing lithium-ion batteries for wearable or household grid storage. Overall, this idea sheds light on the creative problem-solving of future scrap produced during the manufacture of 3D-printed electronic devices. The case study suggests that point-of-use upcycling is the creative solution to utilize conducting 3D printing scrap for a variety of electrochemical devices and applications.

4. Experimental section

4.1 Materials

The scrap of the conductive CNF/PLA filament of Black Magic 3D, USA, was collected from our laboratory. Activated carbon, iodine, sodium hydroxide, block-copolymer P123 (M_w: 6600 g mol^{-1}), potassium iodide (99%), ZnSO$_4$·7H$_2$O, and zinc metal source electrodes (99.99%, 1 mm thick) were purchased from Sigma-Aldrich. The Whatman glass microfiber separator was purchased from Thermo Fisher, Czech Republic.

4.2 Upcycling of CNF/PLA filament scrap and fabrication of electrodes

The gathered scrap from 3D printing, which included threads, fibers, and random fragments, was ground into an average of ~2–3 mm^2 pieces using a traditional mechanical blender. The filament extruder (Felfil Evo, Italy) was filled with these components and set to extrude 1.75 mm diameter filaments at 175 °C and 8–9 screw rotations per minute (rpm). The electrode models were created with Autodesk Fusion 360 software, and a .gcode file for 3D printing was obtained by slicing the .stl drawing file with Prusa Slicer software. With a nozzle temper-ature of 215 °C and a bed temperature of 60 °C, a 3D printer (Prusa i3 MK3, Czech Republic) was used to complete the printing. Furthermore, the 3D-printed CNF/PLA electrode was chemically activated in 4 M NaOH for one hour to eliminate surface PLA and washed with distilled water followed by drying at 60 °C. This electrode termed CNF/PLA@A was used as a cathode host or cathode. A CNF/PLA@Zn anode was prepared by zinc electrodeposition on a CNF/PLA@A in 2 M ZnSO$_4$ aqueous solution with a capacity of 3.3 mA h cm^{-2} at a rate of 40 mA cm^{-2}. The working electrode was CNF/PLA@A, and the zinc plate was taken as a common counter and reference electrode.

4.3 Preparation of polymer gel catholyte (PGC) and polymer gel electrolyte (PGE)

The aqueous catholyte solution was prepared with a mixed concentration of KI (1 M) and I_2 (0.1 M). To convert the liquid

11812 | J. Mater. Chem. A, 2025, 13, 11804–11816

This journal is © The Royal Society of Chemistry 2025

catholyte into PGC, 35 wt% P123 block-copolymer was added to the catholyte solution and allowed to mix properly through three sol–gel cycles at −10 °C to 25 °C. For PGE, 35 wt% P123 was dissolved in 1 M ZnSO₄ following a similar procedure to PGC.

4.4 ZIB configurations

4.4.1. Liquid electrolyte-based ZIBs and symmetrical cells. Circular disk-shaped electrodes with an 8.0 mm diameter and a height of 1.0 mm were fabricated for testing in Swagelok-type cells. For symmetrical cells, 2 M ZnSO₄ electrolyte was used, and a glass fiber separator was placed between two CNF/PLA@Zn anodes. In the case of liquid electrolyte-based ZIBs, the CNF/PLA@A electrode was coated with an activated carbon@iodine composite (1.8 mg cm⁻²) using a carboxymethyl cellulose binder. 2 M ZnSO₄ electrolyte and a glass fiber separator were used. The CNF/PLA@Zn material served as the anode. The carbon-embedded iodine composite was prepared by the solution adsorption method by stirring activated carbon and iodine powder in an aqueous solution for 12 h. Then, iodine adsorbed activated carbon was separated from the aqueous solution and dried at 60 °C for 12 h and termed carbon@iodine. Thermogravimetric analysis confirmed that ∼47 wt% iodine is embedded in carbon powder (Fig. S20†).

4.4.2. PGC/PGE-based ZIBs. ∼20 mg of PGC, which corresponds to an iodine plating density of approximately 1.97 mg cm⁻², was layered onto the CNF/PLA@A to fabricate the cathode. Next, a layer of PGE infused with cellulose was placed on top of the PGC. Finally, the ZIB was completed by placing a CNF/PLA@Zn on the PGE. The entire setup was then tested within a Swagelok cell.

4.4.2.1. Ring-shaped 3D-ZIBs. A ring-shaped CNF/PLA@A in concave geometry and a CNF/PLA@Zn in convex geometry were fabricated. First, PGC (∼50 mg, with an iodine content of 4.94 mg) and PGE were placed in the CNF/PLA@A cavity and then covered with CNF/PLA@Zn. Silicon glue was used as the sealant and insulator between the electrodes. The battery had a total volume of 0.829 cm³. Electrical contact for electrochemical measurement was extended by copper tape.

4.4.2.2. Brick-shaped 3D-ZIBs. Brick-shaped ZIBs (volume, 0.810 cm³; *L*, 1.8 cm; *W*, 0.9 cm; *h*, 0.5 cm; gross weight, 1.012 g) were fabricated using a method to that of ring-shaped batteries except that the electrode shape was a rectangular empty box for CNF/PLA@A and a T-shaped cover for CNF/PLA@Zn. The loading of PGC was ∼50 mg (iodine content, 4.94 mg) in the brick device. The device was rested for 12 h before the measurements began.

4.5 Material characterization

TGA and DSC were performed on a STA200, HITACHI, Japan. Resistivity measurements were conducted on the Ossila Four-Point Probe equipment and using software Ossila Sheet Resistance Lite. Surface analysis was done with SEM (MIRA 3 XMU, Tescan), and EDS mapping and performed using an EDS detector (Oxford Instruments). XRD measurements of electrodes were done using a SmartLab 3 kW diffractometer

(Rigaku), with Cu Kα radiation (λ = 1.54184 Å). The XPS study was done using an AXIS Supra instrument from Kratos Analytical (Manchester, UK) with monochromatized Al Kα excitation (1486.7 eV) with pass energies of 100 eV and 20 eV for the acquisition of survey and high-resolution spectra, respectively. The binding energies were calibrated to the C 1s peak. The *in situ* analysis of the CNF/PLA@A and PGC interface was performed with a Witec Alpha 300R (WITEC-RAMAN) microscope using an excitation wavelength of 532 nm.

4.6 Electrochemical measurements

Electrodeposition measurements and cyclic voltammetry were performed on an electrochemical workstation (AutoLab) and data analysis was done using Nova 2.1 software. Galvanostatic charge–discharge (GCD) and zinc stripping–plating measurements were done using a Land battery tester. The specific capacity, volumetric capacity, and energy density were calculated, respectively, according to eqn (1)–(3):

$$\text{Specific capacity: } C_a = I \times t/3600 \times m \text{ (mA h g}^{-1}\text{)}, \quad (1)$$

$$\text{Volumetric capacity: } C_v = C_a \times \rho \text{ (mA h cm}^{-3}\text{)} \quad (2)$$

$$\text{Energy density: } E_a = C_a \times V \text{ (W h kg}^{-1}\text{)}, \quad (3)$$

where I is the discharge current, t is the discharge time, V is the middle discharge voltage, m is the mass of iodine, and ρ is the density of the ZIB.

Data availability

The data that support the findings of this study are available at zenodo.org.

Author contributions

K. K. Sonigara: material preparation, device fabrication, electrochemistry, data analysis, writing of the original draft; J. V. Vaghasiya: SEM and EDS measurements, 3D printing processes, gadget resources, wring of the original draft; C. C. Mayorga-Martinez: conceptualization, revision of the original draft; M. Pumera: financial support, methodology, supervision, initiation and overseeing of the project. All authors contributed to writing the manuscript.

Conflicts of interest

The authors declare no competing financial or non-financial interests.

Acknowledgements

This journal is © The Royal Society of Chemistry 2025

J. Mater. Chem. A, 2025, **13**, 11804–11816 | **11813**

References

1 M. Zastrow, 3D printing gets bigger, faster, and stronger, *Nature*, 2020, **578**, 20.

2 Y. Y. C. Choong, H. W. Tan, D. C Patel, W. T. N. Choong, C.-H. Chen, H. Y. Low, M. J. Tan, C. D. Patel and C. K. Chua, The global rise of 3D printing during the COVID-19 pandemic, *Nat. Rev. Mater.*, 2020, **5**, 637.

3 G. Rasiya, A. Shukla and K. Saran, Additive Manufacturing-A Review, *Mater. Today: Proc.*, 2021, **47**, 6896–6901.

4 https://www.marketsandmarkets.com/Market-Reports/3d-printing-market-1276.html, accessed, March, 2025.

5 S. C. Daminabo, S. Goel, S. A. Grammatikos, H. Y. Nezhad and V. K. Thakur, Fused deposition modeling-based additive manufacturing (3D printing): techniques for polymer material systems, *Mater. Today Chem.*, 2020, **16**, 100248.

6 *Creating a closed loop supply chain for 3D printing filaments*, HSSMI, https://www.hssmi.org/wp-content/uploads/2021/12/Creating-a-ClosedLoop_case-study.pdf, accessed, November 2023.

7 L. Sandanamsamy, W. S. W. Harun, I. Ishak, F. R. M. Romlay, K. Kadirgama, D. Ramasamy, S. R. A. Idris and F. Tsumori, A comprehensive review on fused deposition modelling of polylactic acid, *Prog. Addit. Manuf.*, 2023, **8**, 775.

8 G. Chyr and J. M. DeSimone, Review of high-performance sustainable polymers in additive manufacturing, *Green Chem.*, 2023, **25**, 453.

9 *The UK 3D Printing Filament Market in 2021*, https://www.filamentive.com/the-uk-3d-printing-filament-market/, accessed, March 2025.

10 *How Much Plastic waste does 3D Printing Really Generate?*, https://www.filamentive.com/how-much-plastic-waste-does-3d-printing-really-generate/, accessed, March 2025.

11 Exploring PLA 3D Printing waste Management and Recycling, *Sustainable 3D Printing Guide*, https://www.linkedin.com/pulse/exploring-pla-3d-printing-waste-management-recycling-ravi-toor/, accessed, March 2025.

12 A. Chamas, H. Moon, J. Zheng, Y. Qiu, T. Tabassum, J. H. Jang, M. Abu-Omar, S. L. Scott and S. Suh, Degradation Rates of Plastics in the Environment, *ACS Sustainable Chem. Eng.*, 2020, **8**, 3494.

13 C. Sun, S. Wei, H. Tan, Y. Huang and Y. Zhang, Progress in upcycling polylactic acid waste as an alternative carbon source: a review, *Chem. Eng. J.*, 2022, **446**, 136881.

14 D. Hidalgo-Carvajal, Á. H. Muñoz, J. J. Garrido-González, R. Carrasco-Gallego and V. A. Montero, Recycled PLA for 3D Printing: A Comparison of Recycled PLA Filaments from Waste of Different Origins after Repeated Cycles of Extrusion, *Polymers*, 2023, **15**, 3651.

15 N. Hayagan, I. Gaalich, P. Loubet, L. Croguennec, C. Aymonier, G. Philippot and J. Olchowka, Challenges and Perspectives for Direct Recycling of Electrode Scraps and End-of-Life Lithium-ion Batteries, *Batteries Supercaps*, 2024, e202400120.

16 B. Hüner, M. Kıstı, S. Uysal, İ. N. Uzgören, E. Özdoğan, Y. O. Süzen, N. Demir and M. F. Kaya, An Overview of Various Additive Manufacturing Technologies and Materials for Electrochemical Energy Conversion Applications, *ACS Omega*, 2022, **7**, 40638.

17 C. W. Foster, M. P. Down, Y. Zhang, X. Ji, S. J. Rowley-Neale, G. C. Smith, P. J. Kelly and C. E. Banks, 3D Printed Graphene Based Energy Storage Devices, *Sci. Rep.*, 2017, **7**, 42233.

18 C. Reyes, R. Somogyi, S. Niu, M. A. Cruz, F. Yang, M. J. Catenacci, C. P. Rhodes and B. J. Wiley, Three-Dimensional Printing of a Complete Lithium Ion Battery with Fused Filament Fabrication, *ACS Appl. Energy Mater.*, 2018, **1**, 5268.

19 E. Redondo, J. Muñoz and M. Pumera, Green Activation Using Reducing Agents of Carbon-based 3D Printed Electrodes: Turning Good Electrodes to Great, *Carbon*, 2021, **175**, 413–419.

20 K. Ghosh, S. Ng, C. Iffelsberger and M. Pumera, Inherent Impurities in Graphene/Polylactic Acid Filament Strongly Influence on the Capacitive Performance of 3D-Printed Electrode, *Chem.–Eur. J.*, 2020, **26**, 15746–15753.

21 C. Iffelsberger, C. W. Jellett and M. Pumera, 3D Printing Temperature Tailors Electrical and Electrochemical Properties through Changing Inner Distribution of Graphite/Polymer, *Small*, 2021, **17**, 2101233.

22 W. Gao and M. Pumera, 3D Printed Nanocarbon Frameworks for Li-Ion Battery Cathodes, *Adv. Funct. Mater.*, 2021, **31**, 2007285.

23 W. Gao, J. Michalička and M. Pumera, Hierarchical Atomic Layer Deposited V_2O_5 on 3D Printed Nanocarbon Electrodes for High-Performance Aqueous Zinc-Ion Batteries, *Small*, 2022, **18**, 2105572.

24 W. Gao, C. Iffelsberger and M. Pumera, Dual polymer engineering enables high-performance 3D printed Zn-organic battery cathodes, *Appl. Mater. Today*, 2022, **28**, 101515.

25 M. Palacios-Corella, K. Ghosh, E. Redondo and M. Pumera, Polyoxometalate-Enhanced 3D-Printed Supercapacitors, *ChemSusChem*, 2022, **15**, e202201490.

26 E. Redondo and M. Pumera, MXene-functionalised 3D-Printed Electrodes for Electrochemical Capacitors, *Electrochem. Commun.*, 2021, **124**, 106920.

27 S. Ng, K. Ghosh, J. Vyskocil and M. Pumera, Two-Dimensional Vanadium Sulfide Flexible Graphite/Polymer Films for Near-infrared Photoelectrocatalysis and Electrochemical Energy Storage, *Chem. Eng. J.*, 2022, **435**, 135131.

28 K. Ghosh and M. Pumera, Free-standing Electrochemically Coated MoS_x Based 3D-Printed Nanocarbon Electrode for

11814 | *J. Mater. Chem. A*, 2025, **13**, 11804–11816

This journal is © The Royal Society of Chemistry 2025

Solid-State Supercapacitor Application, *Nanoscale*, 2021, **13**, 5744–5756.

29 J. V. Vaghasiya, C. C. Mayorga-Martinez and M. Pumera, Smart Energy Bricks: Ti_3C_2@Polymer Electrochemical Energy Storage inside Bricks by 3D Printing, *Adv. Funct. Mater.*, 2021, **31**, 2106990.

30 D. Lin and Y. Li, Recent Advances of Aqueous Rechargeable Zinc-Iodine Batteries: Challenges, Solutions, and Prospects, *Adv. Mater.*, 2022, **34**, 2108856.

31 G. Chen, Y. Kang, H. Yang, M. Zhang, J. Yang, Z. Lv, Q. Wu, P. Lin, Y. Yang and J. Zhao, Toward Forty Thousand-Cycle Aqueous Zinc-Iodine Battery: Simultaneously Inhibiting Polyiodides Shuttle and Stabilizing Zinc Anode through a Suspension Electrolyte, *Adv. Funct. Mater.*, 2023, 2300656.

32 K. K. Sonigara, J. V. Vaghasiya and M. Pumera, Corrosion-Resistant Shape-Programmable $Zn–I_2$ Battery, *Adv. Energy Mater.*, 2024, 2401321.

33 Y. Ji, J. Xie, Z. Shen, Y. Liu, Z. Wen, L. Luo and G. Hong, Advanced Zinc–Iodine Batteries with Ultrahigh Capacity and Superior Rate Performance Based on Reduced Graphene Oxide and Water-in-Salt Electrolyte, *Adv. Funct. Mater.*, 2023, **33**, 2210043.

34 X. Jin, L. Song, C. Dai, Y. Xiao, Y. Han, X. Li, Y. Wang, J. Zhang, Y. Zhao, Z. Zhang, N. Chen, L. Jiang and L. Qu, A Flexible Aqueous Zinc–Iodine Microbattery with Unprecedented Energy Density, *Adv. Mater.*, 2022, **34**, 2109450.

35 D. Yu, A. Kumar, T. A. Nguyen, M. T. Nazir and G. Yasin, High-Voltage and Ultrastable Aqueous Zinc–Iodine Battery Enabled by N-Doped Carbon Materials: Revealing the Contributions of Nitrogen Configurations, *ACS Sustainable Chem. Eng.*, 2020, **8**, 13769.

36 Y. Zou, T. Liu, Q. Du, Y. Li, H. Yi, X. Zhou, Z. Li, L. Gao, L. Zhang and X. Liang, A Four-electron $Zn-I_2$ Aqueous Battery Enabled by Reversible $I^-/I_2/I^+$ Conversion, *Nat. Commun.*, 2021, **12**, 170.

37 F. Yang, J. Long, J. A. Yuwono, H. Fei, Y. Fan, P. Li, J. Zou, J. Hao, S. Liu, G. Liang, Y. Lyu, X. Zheng, S. Zhao, K. Davey and Z. Guo, Single atom catalysts for triiodide adsorption and fast conversion to boost the performance of aqueous zinc–iodine batteries, *Energy Environ. Sci.*, 2023, **16**, 4630.

38 M. Schneider, N. Fritzsche, A. Puciul-Malinowska, A. Baliś, A. Mostafa, I. Bald, S. Zapotoczny and A. Taubert, Surface Etching of 3D Printed Poly(lactic acid) with NaOH: A Systematic Approach, *Polymers*, 2020, **12**(8), 1711.

39 D. Joshy, S. B. Narendranath, Y. A. Ismail and P. Periyat, Recent progress in one dimensional TiO_2 nanomaterials as photoanodes in dye-sensitized solar cells, *Nanoscale Adv.*, 2022, **4**, 5202.

40 H. Zhang, Y. Zhong, J. Li, Y. Liao, J. Zeng, Y. Shen, L. Yuan, Z. Li and Y. Huang, Inducing the Preferential Growth of Zn (002) Plane for Long Cycle Aqueous Zn-Ion Batteries, *Adv. Energy Mater.*, 2023, **13**(1), 2203254.

41 Q. Li, L. Han, Q. Luo, X. Liu and J. Yi, Towards Understanding the Corrosion Behavior of Zinc-Metal Anode in Aqueous Systems: From Fundamentals to Strategies, *Batteries Supercaps*, 2022, **5**(4), e202100417.

42 H. Beydaghi, S. Abouali, S. B. Thorat, A. E. D. R. Castillo, S. Bellani, S. Lauciello, S. Gentiluomo, V. Pellegrini and F. Bonaccorso, 3D printed silicon-few layer graphene anode for advanced Li-ion batteries, *RSC Adv.*, 2021, **11**, 35051.

43 A. Maurel, M. Courty, B. Fleutot, H. Tortajada, K. Prashantha, M. Armand, S. Grugeon, S. Panier and L. Dupont, Highly Loaded Graphite–Polylactic Acid Composite-Based Filaments for Lithium-Ion Battery Three-Dimensional Printing, *Chem. Mater.*, 2018, **30**, 21.

44 A. Maurel, S. Grugeon, B. Fleutot, M. Courty, K. Prashantha, H. Tortajada, M. Armand, S. Panier and L. Dupont, Three-Dimensional Printing of a $LiFePO_4$/Graphite Battery Cell *via* Fused Deposition Modeling, *Sci. Rep.*, 2019, **9**, 18031.

45 M. Idrees, S. Batool, J. Cao, M. S. Javed, S. Xiong, C. Liu and Z. Chen, 3D printed PC/SiOC@Zn hybrid composite as dendrite-free anode for Zn-Ion battery, *Nano Energy*, 2022, **100**, 107505.

46 X. Hu, Y. Chen, W. Xu, Y. Zhu, D. Kim, Y. Fan, B. Yu and Y. Chen, 3D-Printed Thermoplastic Polyurethane Electrodes for Customizable, Flexible Lithium-Ion Batteries with an Ultra-Long Lifetime, *Small*, 2023, **19**(3), 2301604.

47 J. Wang, J. Polleux, J. Lim and B. Dunn, Pseudocapacitive Contributions to Electrochemical Energy Storage in TiO_2 (Anatase) Nanoparticles, *J. Phys. Chem. C*, 2007, **111**(40), 14925–14931.

48 J. Zhao, K. K. Sonigara, J. Li, J. Zhang, B. Chen, J. Zhang, S. S. Soni, X. Zhou, G. Cui and L. Chen, A Smart Flexible Zinc Battery with Cooling Recovery Ability, *Angew. Chem., Int. Ed.*, 2017, **16**, 7871.

49 K. K. Sonigara, J. Zhao, H. K. Machhi, G. Cui and S. S. Soni, Self-Assembled Solid-State Gel Catholyte Combating Iodide Diffusion and Self-Discharge for a Stable Flexible Aqueous $Zn–I_2$ Battery, *Adv. Energy Mater.*, 2020, **10**, 2001997.

50 K. K. Sonigara, H. K. Machhi, J. V. Vaghasiya, A. Gibaud, S. C. Tan and S. S. Soni, A Smart Flexible Solid State Photovoltaic Device with Interfacial Cooling Recovery Feature through Thermoreversible Polymer Gel Electrolyte, *Small*, 2018, **14**, 1800842.

51 J.-L. Yang, H.-H. Liu, X.-X. Zhao, X.-Y. Zhang, K.-Y. Zhang, M.-Y. Ma, Z.-Y. Gu, J.-M. Cao and X.-L. Wu, Janus Binder Chemistry for Synchronous Enhancement of Iodine Species Adsorption and Redox Kinetics toward Sustainable Aqueous $Zn–I_2$ Batteries, *J. Am. Chem. Soc.*, 2024, **146**, 6628.

52 Z. Lv, Y. Kang, G. Chen, J. Yang, M. Chen, P. Lin, Q. Wu, M. Zhang, J. Zhao and Y. Yang, Stable Solid-State Zinc–Iodine Batteries Enabled by an Inorganic $ZnPS_3$ Solid Electrolyte with Interconnected Zn^{2+} Migration Channels, *Adv. Funct. Mater.*, 2024, **34**(3), 2310476.

53 W. Shang, J. Zhu, Y. Liu, L. Kang, S. Liu, B. Huang, J. Song, X. Li, F. Jiang, W. Du, Y. Gao and H. Luo, Establishing High-Performance Quasi-Solid Zn/I_2 Batteries with Alginate-Based Hydrogel Electrolytes, *ACS Appl. Mater. Interfaces*, 2021, **13**(21), 24756.

54 F. Wang, J. Tseng, Z. Liu, P. Zhang, G. Wang, G. Chen, W. Wu, M. Yu, Y. Wu and X. Feng, A Stimulus-Responsive

This journal is © The Royal Society of Chemistry 2025

J. Mater. Chem. A, 2025, **13**, 11804–11816 | 11815

Zinc–Iodine Battery with Smart Overcharge Self-Protection Function, *Adv. Mater.*, 2020, **32**, 2000287.

55 H. K. Machhi, K. K. Sonigara, S. N. Bariya, H. P. Soni and S. S. Soni, Hierarchically Porous Metal–Organic Gel Hosting Catholyte for Limiting Iodine Diffusion and Self-Discharge Control in Sustainable Aqueous Zinc–I_2 Batteries, *ACS Appl. Mater. Interfaces*, 2021, **13**(18), 21426.

56 L. Ma, G. Zhu, Z. Wang, A. Zhu, K. Wu, B. Peng, J. Xu, D. Wang and Z. Jin, Long-Lasting Zinc–Iodine Batteries with Ultrahigh Areal Capacity and Boosted Rate Capability Enabled by Nickel Single-Atom Electrocatalysts, *Nano Lett.*, 2023, **23**, 5272.

57 A. Spadoni, M. Falconieri, M. Lanchi, R. Liberatore, M. Marrocco, G. S. Sau and P. Tarquini, Iodine compounds speciation in HI–I_2 aqueous solutions by Raman spectroscopy, *Int. J. Hydrogen Energy*, 2012, **37**, 1326.

58 J.-X. Lin, J. Liang, J.-F. Feng, B. Karadeniz, J. Lü and R. Cao, Iodine uptake and enhanced electrical conductivity in a porous coordination polymer based on cucurbit[6]uril, *Inorg. Chem. Front.*, 2016, **3**, 1393.

59 X. Li, N. Li, Z. Huang, Z. Chen, G. Liang, Q. Yang, M. Li, Y. Zhao, L. Ma, B. Dong, Q. Huang, J. Fan and C. Zhi, Enhanced Redox Kinetics and Duration of Aqueous I_2/I^- Conversion Chemistry by MXene Confinement, *Adv. Mater.*, 2021, **33**, 2006897.

60 K. K. Sonigara, J. V. Vaghasiya, C. C. Mayorga-Martinez and M. Pumera, Flexible aqueous Zn–S battery based on an S-decorated $Ti_3C_2T_x$ cathode, *npj 2D Mater. Appl.*, 2023, **7**, 45.

61 D. Rahmatabadi, I. Ghasemi, M. Baniassadi, K. Abrinia and M. Baghani, 3D printing of PLA-TPU with different component ratios: fracture toughness, mechanical properties, and morphology, *J. Mater. Res. Technol.*, 2022, **21**, 3970–3981.

62 D. Rahmatabadi, A. Bayati, M. Khajepour, K. Mirasadi, I. Ghasemi, M. Baniassadi, K. Abrinia, M. Bodaghi and M. Baghani, Poly(ethylene terephthalate) glycol/carbon black composites for 4D printing, *Mater. Chem. Phys.*, 2024, **325**, 129737.

11816 | *J. Mater. Chem. A*, 2025, **13**, 11804–11816

This journal is © The Royal Society of Chemistry 2025